

Realization of a fast triple-magic all-optical qutrit in ^{88}Sr

Maximilian Ammenwerth,^{1,2} Hendrik Timme,^{1,2} Flavien Gyger,^{1,2}
Renhao Tao,^{1,2,3} Immanuel Bloch,^{1,2,3} and Johannes Zeiher^{1,2,3,*}

¹*Max-Planck-Institut für Quantenoptik, 85748 Garching, Germany*

²*Munich Center for Quantum Science and Technology (MCQST), 80799 Munich, Germany*

³*Fakultät für Physik, Ludwig-Maximilians-Universität, 80799 Munich, Germany*

(Dated: November 6, 2024)

The optical clock states of alkaline earth and alkaline earth-like atoms are the fundament of state-of-the-art optical atomic clocks. An important prerequisite for the operation of optical clocks are magic trapping conditions, where electronic and motional dynamics decouple. Here, we identify and experimentally demonstrate simultaneous magic trapping for two clock transitions in ^{88}Sr , realizing so-called triple-magic conditions at a specially chosen magic angle. Under these conditions, we operate an all-optical qutrit comprising the ground state 1S_0 , and the two metastable clock states 3P_0 and 3P_2 . We demonstrate fast optical control in an atom array using two- and three-photon couplings to realize high-fidelity manipulation between all qutrit states. Furthermore, at the magic angle we measure atom-atom coherence times between the metastable states as long as 773(21) ms. Our work opens several new directions, including qutrit-based quantum metrology on optical transitions and high-fidelity and high-coherence manipulation on the ^{88}Sr fine-structure qubit.

The vast majority of quantum information and quantum metrology protocols relies on binary representations of quantum information in terms of qubits. For example, efficient interferometry sequences have been devised in quantum metrology that translate phase information into measurable qubit populations [1–3]. Similarly, universal gate sets are known for qubits in quantum computation [4–8], and error correction architectures for qubits are well studied [9–12]. In practice, however, most quantum systems feature more states, which, if controlled, can serve as valuable resources [13–15]. Examples include motional states in trapped atoms or ions or additional internal states that extend the Hilbert space beyond the qubit subspace [16, 17]. The optical clock states of ^{88}Sr are particularly interesting for applications in quantum computing [18, 19] and metrology [3, 20]. So far, most experiments have used the 3P_0 state, coupled to the electronic ground-state 1S_0 at a wavelength of 698 nm as an optical qubit. However, ^{88}Sr features a much richer structure, including the metastable 3P_2 state, which has a predicted natural lifetime exceeding 100 s, providing a second clock transition at 671 nm when coupled to the ground-state 1S_0 [21]. In principle, control over the three transitions coupling the metastable states 3P_0 , 3P_2 and 1S_0 thus provides access to an all-optical qutrit, where all states are split by optical frequencies and can be coupled by laser drives. Experimentally, beyond the well-studied $^1S_0 \leftrightarrow ^3P_0$ transition, coherent manipulation of the 3P_2 state was demonstrated [22]. Furthermore, recent work has explored the fine-structure qubit, which involves only the metastable clock states $^3P_0 \leftrightarrow ^3P_2$ [23, 24]. Going beyond the qubit paradigm in ^{88}Sr and realizing a highly coherent all optical qutrit requires “magic trapping”, where differential light shifts induced by the trapping light vanish and internal and external motional degrees of freedom decouple. Such exper-

imentally fine-tuned magic trapping conditions have been demonstrated for various optical transitions in alkaline-earth (like) atoms by tuning the angle between the trap polarization and the quantization axis defined by a magnetic field [25–27], or ellipticity of the trap polarization with respect to the quantization axis [22, 23, 28]. Even at magic trapping conditions, an experimental difficulty in coupling the optical clock states, in particular in bosonic ^{88}Sr , is the requirement for large laser power in combination with strong magnetic fields [29]. This severe experimental limitation can be mitigated by employing a three-photon coupling scheme [30], which was recently demonstrated for the $^1S_0 \leftrightarrow ^3P_0$ transition using a Bose-Einstein condensate [31] and a thermal cloud of strontium atoms [32].

Here, we significantly expand on previous work and demonstrate an array of optical qutrits encoded in the absolute ground state 1S_0 and both metastable clock states 3P_0 , 3P_2 of ^{88}Sr , and trapped in an optical tweezer array. Our work relies on tuning to simultaneous magic trapping conditions at a trap wavelength of 813 nm for the ground state and both clock states. At magic conditions, we couple all involved states via multi-photon transitions, which allow for fast all-to-all Rabi coupling at relatively low magnetic fields. We benchmark the atom-laser coherence of the fine-structure qubit and reach T_2 times up to $\tau_{dd} = 345(12)$ ms under continuous dynamical decoupling, significantly exceeding the previous state of the art. We furthermore find a lower bound of the atom-atom coherence time for the fine-structure qubit as long as $\tau_{at} = 773(21)$ ms, which is on par with coherence times achievable with ground hyperfine states in alkali atoms [33, 34]. Our work thus demonstrates the potential scalability of qubits encoded in the metastable manifold of strontium atoms.

To realize triple-magic trapping conditions, we choose

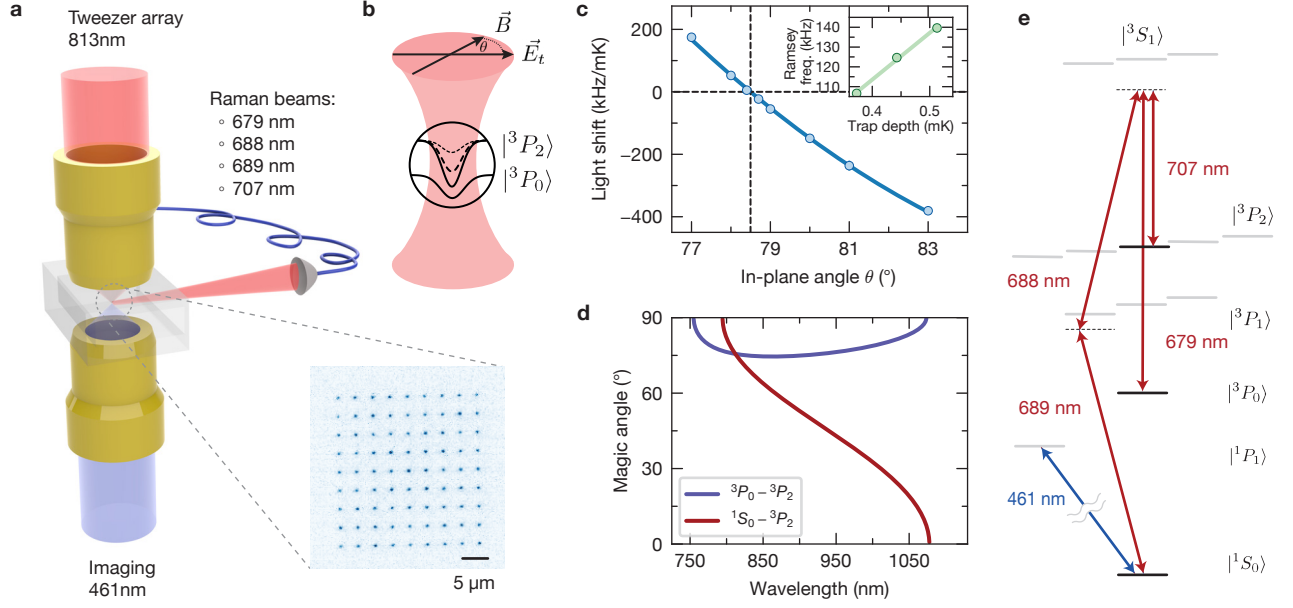


FIG. 1. **Realization of triple-magic trapping conditions.** **a** Main features of our experimental setup. We generate tweezer arrays at a wavelength of 813 nm using the top objective and image the atoms onto a camera using the bottom objective. Coherent control over the qutrit states is realized with four light fields at 679 nm, 688 nm, 689 nm, and 707 nm, which are delivered with common linear polarization from the same optical fiber and focussed onto the tweezer array. **b** Trapped in the optical tweezer, the two clock states a priori experience different trapping potential with a strong contribution of the tensor-polarizability. By choosing a suitable angle of the magnetic field with respect to the tweezer polarization we equalize the polarizability as described in the main text. **c** The differential light shift between the clock states obtained from Ramsey spectroscopy is shown as a function of the magnetic field angle. The dependence of the differential light-shift on tweezer depth is shown as a function of trap depth in the inset for a specific magnetic field in-plane angle of 81° . **d** The expected magic angle is shown as function of wavelength. At 813 nm the 1S_0 and 3P_0 state are scalar-magic which therefore enables triple-magic conditions. **e** Level diagram of ^{88}Sr and the relevant wavelength used in this work. To drive three-photon transitions, we choose a detuning in the vicinity of the $^1S_0 \leftrightarrow ^3P_{1,m_j=-1}$ resonance.

our tweezer wavelength at 813 nm to provide magic trapping conditions between the ground-state 1S_0 and the clock state 3P_0 [35, 36]. In addition, we tune the polarizability of the 3P_2 state to the same value, which can be achieved in ^{88}Sr for the $^3P_2, m_j = 0$ state by applying a magnetic field under an angle θ with respect to the linear tweezer polarization, in analogy to the known strategy for 3P_1 [25]. Due to the absence of total angular momentum J in the ground and 3P_0 clock states, their polarizability is unchanged by applying a magnetic field. We thus obtain the following expression for the tunable differential polarizability between 1S_0 , 3P_0 and 3P_2

$$\Delta\alpha = 3(\alpha_1 - \alpha_0)\sin^2\theta + \alpha_0, \quad (1)$$

with $\alpha_i = \alpha_{^3P_0} - \alpha_{^3P_2, m_j=i}$ being the polarizability difference between the $J = 0$ states and the $m_j = i$ Zeeman state of 3P_2 . Using the known polarizability data for strontium, magic-angle tuning should enable the realization of magic trapping conditions across a wide range of wavelengths, see Fig. 1d.

In our experiment, we operate a 9×9 site tweezer array at a wavelength of 813 nm in the focal plane of a

high-resolution objective, see Fig. 1a. Our experimental sequence starts by loading the tweezer array from a two-stage magneto-optical trap, followed by a parity projection step to remove double occupancy in the tweezers. Subsequently, we image the occupation of the array by collecting the atomic fluorescence at a wavelength of 461 nm using a second objective and image it onto a qCMOS camera, see Fig. 1a. During the imaging pulse, we additionally employ attractive Sisyphus cooling on the $^1S_0 \leftrightarrow ^3P_1$ transition at 689 nm, resulting in high-fidelity, low-loss detection of the occupation of individual tweezers [37]. After this first image, we apply a sideband cooling pulse to cool the atoms in the radial direction, reaching a mean residual excitation number $\bar{n} = 0.14(4)$ [25] and correspondingly a motional ground-state occupation of 88(3)%. Subsequently, we apply a magnetic field with a strength of 19 G in the horizontal plane at an angle θ between the linearly polarized tweezer array with electric field vector \vec{E}_t and the magnetic quantization axis \vec{B} . At our typical trap depths of $U_0/k_B \leq 0.5$ mK, the chosen field strength is sufficient to define the quantization axis, which is required for magic-angle tuning. To

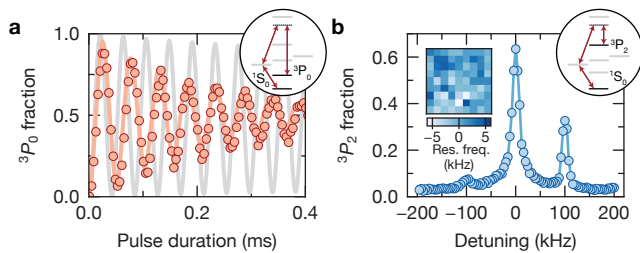


FIG. 2. **Three-photon coupling between 1S_0 and 3P_0 , 3P_2 .** **a** Rabi oscillations between 1S_0 and 3P_0 . The red line shows simulation results of a simplified two-level model based on the measured in-loop laser phase noise without any free parameter. The gray line shows a noise-free simulation of the system taking all Zeeman-substates and their couplings into account (see Appendix). **b** We directly drive the $^1S_0 \leftrightarrow ^3P_2$ transition with a three-photon pulse by substituting the 679 nm light field with a corresponding beam at 707 nm, resulting in narrow resonance features with resolved red and blue motional sidebands. Extracting the center frequency for the $^1S_0 \leftrightarrow ^3P_2$ transition for each tweezer (inset) we compute the tweezer-resolved polarization angle (see Appendix). At a relative detuning of 100 kHz from the carrier we observe the radial sidebands of our tweezer array.

couple 1S_0 to 3P_0 (3P_2), we use a combination of three photons at 689 nm, 688 nm and 679 nm (707 nm), coupling via the intermediate states 3P_1 with a detuning of $|\Delta_{689}| = 2\pi \times 6$ MHz (with respect to $^3P_{1,m_j=-1}$) and 3S_1 with a detuning of $|\Delta_{679}| = 2\pi \times 12$ GHz ($|\Delta_{707}| = 2\pi \times 12$ GHz), see Fig. 1e. We couple the two metastable states $^3P_0 \leftrightarrow ^3P_2$ off-resonantly via 3S_1 at Δ_{679} using two photons at 679 nm and 707 nm. To suppress differential phase noise, all lasers are locked to the same frequency comb and delivered to the experiment using the same polarization maintaining fiber. To locate the position of the magic angle, we first prepare the atoms in the 3P_0 clock state using a fast three-photon transfer [31, 32], further described below. We then measure the light-shift on the $^3P_0 \leftrightarrow ^3P_2$ transition via Ramsey spectroscopy as a function of trap depth at various angles, see Fig. 1c. We find that the differential polarizability vanishes at an angle of $\theta_m = 78.49(3)^\circ$, in good agreement with the expected value considering a systematic uncertainty in the relative angle between tweezer polarization and magnetic field axis given by the coil orientation.

With the magic condition identified, we proceed to demonstrate fast, coherent, all-optical control of all transitions involved in the qutrit. In particular, we use combinations of three photons to couple from the ground state to both metastable states [31, 32], and two photons to couple the two metastable states, as recently demonstrated in trapping conditions different from our experiment [23, 24]. For the qutrit realized here, the combination of multi-photon processes allows for fast all-optical control at relatively modest external magnetic

fields, which dramatically simplifies the experimental requirements to set the magic angle. The multi-color light field is impinging onto the array with linear polarization tilted approximately 55° out of the horizontal plane, which was chosen to equalize the polarization projection of the π and σ^\pm components with respect to the horizontally set magnetic field and which maximizes the three-photon Rabi frequency in this configuration. On three-photon resonance, we observe corresponding Rabi oscillations with an initial contrast (at $\Omega_{3P_0} t = \pi$) reaching up to 88% averaged over 118 repetitions of the experiment and the whole tweezer array, see Fig. 2a. The extracted Rabi frequency of $\Omega_{3P_0} = 2\pi \times 19.16(2)$ kHz for less than 10 mW total power in all three beams agrees well with analytic expectations and numerical simulations discussed in more detail in the Appendix. By modelling the Rabi oscillations in presence of experimental imperfections, we find that the observed dephasing is almost entirely accounted for by the independently measured laser phase noise [38]. Simulating a noise-free quantum system, we find that the limitations imposed by off-resonant scattering from excited states allow for substantially more Rabi cycles before the system dephases, see Fig. 2a. In analogy to the coherent coupling to 3P_0 , we also realize a coherent excitation of the 3P_2 state at the magic angle, by substituting the photon at 679 nm with a photon at 707 nm, see Fig. 2b. Performing high-resolution spectroscopy, we find in this case a tweezer-dependent shift of the resonance position, which we attribute to small imperfections in the alignment of the array optics and a corresponding variation of the tweezer polarization angle across the array. These observations indicate the critical influence of precise alignment and the challenge to realize scalable tweezer arrays with excellent homogeneity.

With fast three-photon control on both ground-to-metastable transitions at hand, we now proceed to characterize the fine-structure (FS) qubit formed by both metastable states coupled on a coherent two-photon transition via the intermediate state 3S_1 in triple-magic conditions. For all measurements described in the following, we initialize the fine-structure qubit via a three-photon π -pulse on the $^1S_0 \leftrightarrow ^3P_0$ transition. Detection is similarly performed by controlled de-excitation of the clock state back into the ground state. Driving Rabi oscillations between 3P_0 and 3P_2 , we extract a Rabi frequency of $\Omega_{FS} = 2\pi \times 117$ kHz using only ~ 900 μ W of power at 707 nm and ~ 850 μ W of power at 679 nm. Here, the polarization setting that optimizes the coherent three-photon preparation is suboptimal, effectively lowering the achievable two-photon coupling on the FS qubit. However, we chose to use this setting for experimental convenience of not having to change the polarization between manipulation of the clock transitions and the FS transition. The FS qubit Rabi oscillations exhibit damping with a $1/e$ time of $50(1)$ μ s, again compatible with estimates computed from the independently measured

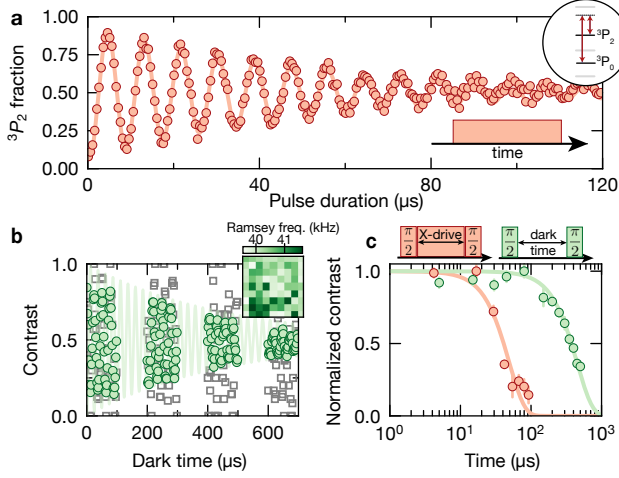


FIG. 3. **Fine-structure qubit under triple-magic conditions.** **a** Rabi oscillations on the fine-structure qubit under triple-magic conditions. We first initialize the qubit with a three-photon pulse into 3P_0 and then drive Rabi oscillations between the fine-structure states. The rapid dephasing is caused by laser phase noise. **b** Tweezer-resolved Ramsey measurement on the fine-structure qubit. The tweezer averaged contrast (green circles) rapidly drops while individual tweezers (gray squares) show a high contrast. The tweezer-dependent Ramsey frequency (inset) is caused by a spatially varying polarization across the tweezer-array (see Appendix). Note that the single tweezer contrast decays on substantially longer timescales. **c** Comparison of the Ramsey measurement (green) with a spin-lock measurement (red). For both measurements, we apply two $\pi/2$ -pulses along the Y-axis separated by waiting time in the dark (green) or under a continuous Rabi drive along the X-axis (red). The contrast of the spin-lock measurement decays significantly faster on a time scale of $\tau_{sl} = 49(4) \mu\text{s}$ in agreement with the contrast decay in the Rabi oscillations, indicating limitations due to laser phase noise. For comparison, the T_2^* measurement on the fine-structure qubit shows a tweezer-averaged contrast decay with an extracted time of $\tau_R = 463(7) \mu\text{s}$.

phase noise. To further substantiate that phase noise dominates the decay dynamics of the Rabi oscillations, we perform a spin lock measurement by first applying a $\pi/2$ -pulse around the Y-axis, which aligns the state along the X-axis in the state $|+\rangle = (|^3P_0\rangle + |^3P_2\rangle)/\sqrt{2}$ followed by a variable-time Rabi drive about the X-axis [39]. In the absence of noise, the X-drive is aligned and should stabilize the state $|+\rangle$. After a second $\pi/2$ -pulse of variable phase, we perform a projective measurement of the populations in 3P_0 and 3P_2 and extract the contrast of the resulting Ramsey fringe. With this sequence, we observe a fast drop of the contrast with a time constant $\tau_{sl} = 49(4) \mu\text{s}$ in presence of the X-drive, which indicates that currently excess phase noise at the Rabi drive is a major source of decoherence for our current lasersystem [40] and limits the observed contrast of our Rabi oscillations [41, 42]. Here, the time constant τ_{sl} is obtained

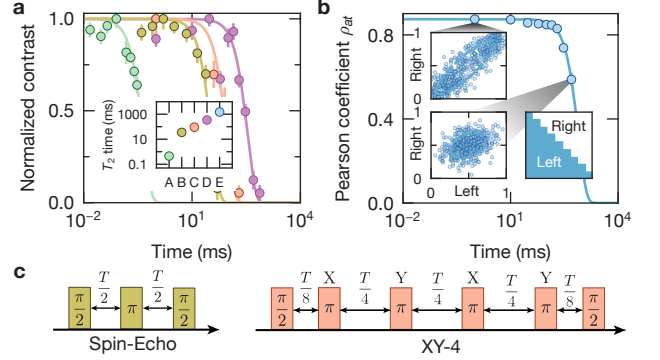


FIG. 4. **Coherence of the fine-structure qubit.** **a** Comparison of the fine-structure qubit T_2^* time and T_2 time measured with a XY-4 dynamical decoupling sequence. At a trap depth of $46 \mu\text{K}$ we obtain a T_2^* time of $\tau_R = 463(7) \mu\text{s}$ (light-green, inset A) and T_2 time of $\tau_{se} = 36(2) \text{ms}$ with a single spin-echo (olive-green, inset B). Using a XY-4 dynamical decoupling sequence the T_2 time becomes $\tau_{dd} = 97(6) \text{ms}$ (orange, inset C) and lowering the tweezer depth to about $5 \mu\text{K}$, we boost the T_2 time to $\tau_{dd} = 346(37) \text{ms}$ (purple, inset D) setting a limit on the atom-laser coherence. The inset shows a summary of the measured coherence times including the atom-atom coherence time (blue, inset E). **b** To benchmark the atom-atom coherence we compute correlations between the left and right half of the tweezer array (see insets). The Pearson correlation coefficient decays with a time constant of $773(21) \text{ms}$. **c** Pulse sequences used to measure the T_2 times using spin-echo and XY-4 dynamical decoupling.

by fitting the resulting contrast with a function of the form $C(t) \propto \exp(-(t/\tau_{sl})^2)$. To further analyze the performance of the FS-qubit, we also study its coherence in the absence of any driving light. Previous work [24] has raised concerns as to the achievable coherence times on the fine-structure qubit due to the presence of spatially dependent differential polarizabilities in tightly focused optical tweezers, which lead to temperature- and trap-depth dependent spin motion coupling. First, we perform a standard Ramsey sequence with two $\pi/2$ -pulses separated by a variable dark-time and obtain a T_2^* time of $\tau_R = 463(7) \mu\text{s}$. A tweezer-resolved analysis of the Ramsey oscillation frequency reveals that this rapid dephasing is dominated by inhomogeneities across the tweezer array, see Fig. 3b. Such inhomogeneous shifts can be mitigated using dynamical decoupling techniques. Employing a standard XY-4 dynamical decoupling sequence, we find a strongly boosted T_2 time of $\tau_{dd} = 345(12) \text{ms}$, exceeding previous measurements in angle- or polarization-tuned magic optical traps by at least an order of magnitude [23, 24]. We further study the limits to the FS-qubit coherence by analyzing correlations between the qubit states measured within two subsystems of the tweezer array, see Fig. 4. This measurement reveals the achievable atom-atom coherence, which can exceed the laser-atom coherence significantly [3]. We extract a decay time of $\tau_{at} = 773(21) \text{ms}$ from a fit to our data, which can be in-

terpreted as a lower bound to the atom-atom coherence achievable for the FS qubit in ^{88}Sr and on par with coherence times achieved e.g., in hyperfine states of alkali atoms [34]. We expect that, with higher quality Rabi oscillations and more dynamical decoupling pulses, the coherence time can be boosted further.

Our first realization and benchmark of a triple-magic qubit in ^{88}Sr opens up new possibilities in quantum computing, quantum simulation and metrology with alkaline-earth atoms. Overcoming the technical limitations associated with laser noise opens the route to quantum computing and quantum simulation architectures involving fast transfers between the highly coherent strontium clock qubit [3] for storage and the fast FS-qubit for operations. Compared to the usually employed single-photon couplings, the three-photon coupling has the distinct advantage of operating at only low to moderate magnetic fields with high Rabi couplings at small required optical powers, dramatically improving the scaling perspectives of this approach. Tuning the two-photon coupling from the FS-qubit on resonance with the 3P_1 state, which subsequently decays to the ground state, can serve as a building block for recently proposed measurement-free quantum error correction [43], or highly controllable dissipative steps required for digital quantum simulation of open systems [44]. Moreover, our promising results on the achievable coherence in angle-tuned magic traps opens interesting perspectives for using the $^1S_0 \leftrightarrow ^3P_2$ qubit, which can conveniently be tuned to magic conditions across a broad wavelength range including IR wavelengths suitable for high-power Ytterbium-doped fiber amplifiers. Finally, our demonstrated atom-atom coherence time involving the 3P_2 state opens promising perspectives for a variety of clock transitions in atoms trapped in non-scalar magic optical traps [45]. Thus, our work sets the stage for quantum metrology applications involving at least two clock transitions, which have been discussed in the context of uncovering slow temporal changes in fundamental constants [46].

We thank Ria Rosenauer and Kevin Mours for help with the 688 nm laser setup and Eran Reches and Lorenzo Festa for the code to estimate phase noise induced limitations. We acknowledge funding by the Max Planck Society (MPG) the Deutsche Forschungsgemeinschaft (DFG, German Research Foundation) under Germany's Excellence Strategy-EXC-2111-390814868, from the Munich Quantum Valley initiative as part of the High-Tech Agenda Plus of the Bavarian State Government, and from the BMBF through the programs MUNIQC-Atoms and MAQCS. This publication has also received funding under Horizon Europe programme HORIZON-CL4-2022-QUANTUM-02-SGA via the project 101113690 (PASQuanS2.1). J.Z. acknowledges support from the BMBF through the program "Quantum technologies - from basic research to market" (SNAQC, Grant No. 13N16265). H.T., M.A. and R.T. acknowledge funding

from the International Max Planck Research School (IMPRS) for Quantum Science and Technology. M.A. acknowledges support through a fellowship from the Hector Fellow Academy. F.G. acknowledges funding from the Swiss National Fonds (Fund Nr. P500PT_203162).

Three-photon coupling

This Appendix provides a brief analytic description of the three-photon coupling including a fidelity estimation obtained after adiabatic elimination of the intermediate excited states. Following ref. [30], we consider a 4-level system and neglect the Zeeman-substructure. In a suitable rotating frame the Hamiltonian is given by

$$\begin{aligned} H/\hbar = & -\Delta_{689}|^3P_1\rangle\langle^3P_1| - (\Delta_{689} + \Delta_{688})|^3S_1\rangle\langle^3S_1| \\ & - (\Delta_{689} + \Delta_{688} - \Delta_{679})|^3P_0\rangle\langle^3P_0| \\ & + \left(\frac{\Omega_{689}}{2}|^1S_0\rangle\langle^3P_1| + \frac{\Omega_{688}}{2}|^3P_1\rangle\langle^3S_1| \right. \\ & \left. + \frac{\Omega_{679}}{2}|^3S_1\rangle\langle^3P_0| + h.c. \right). \end{aligned}$$

Here, Δ_i denotes the detuning from the respective resonance. For example, Δ_{689} denotes the detuning from the $^1S_0 \leftrightarrow ^3P_{1,m_J=-1}$ transition and Δ_{688} (Δ_{679}) denote the detuning from the $^3P_{1,m_J=-1} (^3P_0) \leftrightarrow ^3S_{1,m_J=-1}$ resonance. The Rabi frequencies Ω_i account for the coherent coupling of the multi-chromatic light field and are computed according to Eq. 2. In addition to the unitary coupling described by the Hamiltonian, both intermediate excited states decay due to their finite lifetime which is described by Lindblad decay operators: $L_{ij} = \sqrt{\Gamma_{ij}}|j\rangle\langle i|$ for $i = ^3P_1, ^3S_1$ and $j = ^1S_0, ^3P_0$. We consider decay from 3P_1 back to 1S_0 and decay from 3S_1 to 3P_0 and 3P_1 (which subsequently decays further to 1S_0). This is particularly relevant for the 3S_1 -state which has a lifetime of 13.9(1) ns and consequently a decay rate comparable to the Rabi frequencies on the individual legs [47]. A large detuning with respect to the 3S_1 -state is therefore required to overcome limitations from off-resonant single-photon scattering. Under the combined effect of coherent driving and dissipation the dynamics of our model are described by a Lindblad master equation for a density matrix ρ . We obtain the effective dynamics upon adiabatic elimination of the two intermediate excited states following an effective operator formalism [48]. This provides us with the coherent coupling rates as well as dissipation rates within the ground-state subspace. The effective Hamiltonian for the remaining two-level system contains the three-photon coupling and the single-beam

light shifts

$$H_{\text{eff}}/\hbar = -(\Delta_{689} + \Delta_{688} - \Delta_{679})|^3P_0\rangle\langle^3P_0| \\ + \left(\frac{\Omega_3}{2} |^1S_0\rangle\langle^3P_0| + h.c. \right) \\ + \frac{1}{4} \frac{|\Omega_{689}|^2}{\Delta_{689}} |^1S_0\rangle\langle^1S_0| + \frac{1}{4} \frac{|\Omega_{679}|^2}{\Delta_{679}} |^3P_0\rangle\langle^3P_0|,$$

using the further approximated three-photon Rabi frequency

$$\Omega_3 = \frac{\Omega_{689}\Omega_{688}\Omega_{679}}{4\Delta_{689}\Delta_{679}}.$$

In addition, the effective operator formalism provides effective decay rates between the 1S_0 and 3P_0 states which describe depolarization and dephasing. The two most important contributions describe dephasing due to off-resonant scattering, which we combine to one effective dephasing rate

$$\Gamma_{\text{eff}} = \Gamma_{3P1} \frac{\Omega_{689}^2}{4\Delta_{689}^2} + \Gamma_{3S1} \frac{\Omega_{679}^2}{4\Delta_{679}^2}$$

Additional contributions to dephasing and depolarization are suppressed in comparison to these dominant contributions within our 4-level approximation. We are interested in finding the optimal parameter set in the 5-dimensional parameter space (one detuning is fixed to stay on three-photon resonance) to maximize the fidelity. We find a simple analytic expression for the infidelity under the assumption that the fidelity is optimal if the scattering rates from both excited states are equal. Under this assumption, the infidelity estimate ϵ depends only on the Rabi frequency of the 688 nm beam,

$$\epsilon = \frac{\Gamma_{\text{eff}}}{\Omega_3} = 2\sqrt{\frac{\Gamma_{3P1}}{\Gamma_{3S1}} \frac{\Gamma_{3S1}}{\Omega_{688}}} \approx \frac{1}{19.4} \frac{\Gamma_{3S1}}{\Omega_{688}}.$$

We confirm that this infidelity limit is indeed approximately reached throughout a large volume of the parameter space via numerical simulations of the 4-level system without adiabatic approximation. These simulations are executed on three-photon resonance given by the constraint

$$\Delta_{679} = \Delta_{688} + \Delta_{689} - \frac{1}{4} \left(\frac{\Omega_{679}^2}{\Delta_{679}} - \frac{\Omega_{689}^2}{\Delta_{689}} \right).$$

Since all laser beams participating in the three-photon coupling are delivered from the same optical fiber, they exhibit an approximately equal beam waist at the atomic position. This allows to cancel the three-photon probe shifts using settings for which the differential light shifts vanish:

$$\frac{\Omega_{679}^2}{\Delta_{679}} = \frac{\Omega_{689}^2}{\Delta_{689}}$$

Driving the three-photon coupling requires a polarization with π as well as σ^\pm projection for the individual

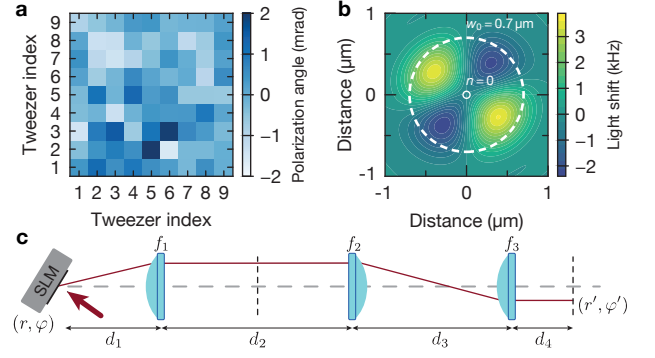


FIG. 5. **Polarization gradients.** **a** Tweezer-resolved polarization angle computed from the tweezer-resolved $^1S_0 \leftrightarrow ^3P_2$ spectroscopy. **b** Due to the high numerical aperture used to focus down the tweezer array, the traps exhibit a spatial polarization gradient. We numerically compute the local polarization and resulting differential energy shift shown here for a central trap depth of $U_0/k_B = 46 \mu\text{K}$ and a magnetic field strength of 19 G. The dashed white ring indicates the waist of our tweezers. The inner solid ring indicates the ground-state root-mean-square value $\sqrt{\langle \hat{x}_{n=0}^2 \rangle}$. **c** Simplified sketch of the SLM setup used to estimate the deviation from a 4f-system and its effect on the polarization gradients across the array.

colors. To maximize the three-photon Rabi frequency in our collinear setup with common polarization, we choose an angle of approximately 55° with respect to the horizontal plane. This configuration provides an equal polarization projection factor of $\frac{1}{\sqrt{3}}$ to each component, which maximizes the three-photon Rabi frequency under the constraint of common polarization. For the numerical simulation shown in Fig. 2a we generalize the Hamiltonian to include all dipole-allowed couplings and compute the corresponding Rabi frequency between states $|J_0, m_0\rangle$ and $|J_1, m_1\rangle$ according to

$$\Omega_i = p_q \cdot E/\hbar \cdot D \cdot \begin{pmatrix} J_0 & 1 & J_1 \\ m_0 & q & -m_1 \end{pmatrix} \\ \times \sqrt{2J_1 + 1} \cdot (-1)^{J_0 + J_1 + J_> - m_1}. \quad (2)$$

Here, p_q is a polarization projection factor, $q = -1, 0, 1$ labels the polarization σ^-, π, σ^+ and $J_>$ denotes the larger value of J_0, J_1 [49]. The Rabi frequency depends on the electric field strength $E = \sqrt{4P/(\pi w_0 c \epsilon_0)}$ for given power P and beam waist w_0 and the reduced dipole matrix element $D = \sqrt{3\epsilon_0 \hbar \lambda_0^3 \Gamma} / (8\pi^2)$ on the transition with the inverse lifetime Γ and the transition wavelength λ_0 . For our multi-level extension we also consider decay from 3S_1 into 3P_2 .

Polarization gradients

The $^1S_0 \leftrightarrow ^3P_2$ three-photon resonance shown in Fig. 2b exhibits a tweezer-dependent resonance shift

which is caused by polarization gradients across the tweezer array. This shift translates to a tweezer-dependent polarization angle that is consistent with a residual axial misalignment of the SLM setup from a 4f-system. The tweezer-dependent resonance shift Δf_{res} at a given trap depth U_0 is converted to a polarization angle correction $\Delta\theta = \frac{\Delta f_{\text{res}}}{U_0} \frac{1}{\nu}$ using the measured slope $\nu = 6.03 \text{ kHz}/(\text{mK mrad})/k_B$ (see Fig. 1c) yielding an angular spread of about $\Delta\theta = \pm 1.6 \text{ mrad}$ across the tweezer array, see Fig. 5a. For a displacement δ of the SLM with respect to a 4f-configuration (see Fig. 5c) the tweezer angle in the atomic plane for a centered input beam ($r = 0$) is given by:

$$\varphi' = \frac{M\varphi}{f_3} \delta \quad (3)$$

For our magnification of $M = \frac{f_2}{f_1} = 3$, the focal length of $f_3 = 24 \text{ mm}$ of the microscope objective and a typical angle distribution of about $\varphi(r) = \frac{r}{f_1} = \pm 2 \text{ mrad}$ at the SLM, this indicates a plausible displacement of $\delta \approx 5.3 \text{ mm}$. Eq. 3 is derived from a simple ABCD-matrix calculation taking into account the free propagation over distances d_i and the lenses with focal length f_i , shown in Fig. 5c. We find that φ' is most sensitive to an error δ on the propagation between the SLM and the first lens considering $d_1 = f_1 + \delta$. The displacement gives rise to a tweezer-dependent polarization tilt out of the horizontal plane, which consequently contributes to a tweezer-dependent light shift that limits the T_2^* time due to inhomogeneous broadening. In addition to polarization gradients across the tweezer array the local polarization within each tweezers is modulated depending on the displacement with respect to the tweezer center because of the high numerical aperture of 0.65 of our microscope objective [50]. The local polarization is computed by numerically solving the vector Debye integrals [51] and subsequently translated to energy shifts by numerically computing the eigenstates given the local polarization and trap depth and the globally applied magnetic field [24, 28]. We find that the effect of polarization gradients within the tweezers is irrelevant for T_2 times on the order of several hundred milliseconds at our trap depth of $U_0/k_B = 5 \text{ } \mu\text{K}$ even in the absence of axial ground-state cooling. To further suppress the effect of locally varying polarization, we envision to trap atom arrays in optical lattices instead of tweezer arrays [52–55].

* johannes.zeiher@mpq.mpg.de

- [1] N. Hinkley, J. A. Sherman, N. B. Phillips, M. Schioppa, N. D. Lemke, K. Beloy, M. Pizzocaro, C. W. Oates, and A. D. Ludlow, An atomic clock with 10^{-18} instability, *Science* **341**, 1215–1218 (2013).
 [2] E. Kessler, P. Kómár, M. Bishof, L. Jiang, A. Sørensen, J. Ye, and M. Lukin, Heisenberg-limited atom clocks

based on entangled qubits, *Phys. Rev. Lett.* **112**, 190403 (2014).

- [3] A. W. Young, W. J. Eckner, W. R. Milner, D. Kedar, M. A. Norcia, E. Oelker, N. Schine, J. Ye, and A. M. Kaufman, Half-minute-scale atomic coherence and high relative stability in a tweezer clock, *Nature* **588**, 408–413 (2020).
 [4] S. Bravyi and A. Kitaev, Universal quantum computation with ideal clifford gates and noisy ancillas, *Phys. Rev. A* **71**, 022316 (2005).
 [5] M. Saffman, Quantum computing with atomic qubits and rydberg interactions: progress and challenges, *J. Phys. B* **49**, 202001 (2016).
 [6] M. Saffman, T. G. Walker, and K. Mølmer, Quantum information with rydberg atoms, *Rev. Mod. Phys.* **82**, 2313–2363 (2010).
 [7] S. J. Evered, D. Bluvstein, M. Kalinowski, S. Ebadi, T. Manovitz, H. Zhou, S. H. Li, A. A. Geim, T. T. Wang, N. Maskara, H. Levine, G. Semeghini, M. Greiner, V. Vuletić, and M. D. Lukin, High-fidelity parallel entangling gates on a neutral-atom quantum computer, *Nature* **622**, 268–272 (2023).
 [8] X.-F. Shi, Deutsch, toffoli, and cnot gates via rydberg blockade of neutral atoms, *Phys. Rev. Applied* **9**, 051001 (2018).
 [9] A. G. Fowler, M. Mariantoni, J. M. Martinis, and A. N. Cleland, Surface codes: Towards practical large-scale quantum computation, *Phys. Rev. A* **86**, 032324 (2012).
 [10] K. Sahay, J. Jin, J. Claes, J. D. Thompson, and S. Puri, High-threshold codes for neutral-atom qubits with biased erasure errors, *Phys. Rev. X* **13**, 041013 (2023).
 [11] E. Knill and R. Laflamme, Theory of quantum error-correcting codes, *Phys. Rev. A* **55**, 900–911 (1997).
 [12] Y. Wu, S. Kolkowitz, S. Puri, and J. D. Thompson, Erasure conversion for fault-tolerant quantum computing in alkaline earth rydberg atom arrays, *Nat. Commun.* **13**, 4657 (2022).
 [13] T. Roy, Z. Li, E. Kapit, and D. Schuster, Two-qutrit quantum algorithms on a programmable superconducting processor, *Phys. Rev. Applied* **19**, 064024 (2023).
 [14] A. R. Shlyakhov, V. V. Zemlyanov, M. V. Suslov, A. V. Lebedev, G. S. Paraoanu, G. B. Lesovik, and G. Blatter, Quantum metrology with a transmon qutrit, *Phys. Rev. A* **97**, 022115 (2018).
 [15] S. Omanakuttan, V. Buchemavari, J. A. Gross, I. H. Deutsch, and M. Marvian, Fault-tolerant quantum computation using large spin-cat codes, *PRX Quantum* **5**, 020355 (2024).
 [16] L. H. Bohnmann, D. F. Locher, J. Zeiher, and M. Müller, Bosonic quantum error correction with neutral atoms in optical dipole traps, (2024), arXiv:2408.14251.
 [17] M. Ringbauer, M. Meth, L. Postler, R. Stricker, R. Blatt, P. Schindler, and T. Monz, A universal qudit quantum processor with trapped ions, *Nat. Phys.* **18**, 1053–1057 (2022).
 [18] N. Schine, A. W. Young, W. J. Eckner, M. J. Martin, and A. M. Kaufman, Long-lived bell states in an array of optical clock qubits, *Nat. Phys.* **18**, 1067–1073 (2022).
 [19] I. S. Madjarov, J. P. Covey, A. L. Shaw, J. Choi, A. Kale, A. Cooper, H. Pichler, V. Schkolnik, J. R. Williams, and M. Endres, High-fidelity entanglement and detection of alkaline-earth rydberg atoms, *Nat. Phys.* **16**, 857–861 (2020).

- [20] A. L. Shaw, R. Finkelstein, R. B.-S. Tsai, P. Scholl, T. H. Yoon, J. Choi, and M. Endres, Multi-ensemble metrology by programming local rotations with atom movements, *Nat. Phys.* **20**, 195–201 (2024).
- [21] J. Trautmann, D. Yankelev, V. Klüsener, A. J. Park, I. Bloch, and S. Blatt, $^1S_0 - ^3P_2$ magnetic quadrupole transition in neutral strontium, *Phys. Rev. Res.* **5**, 013219 (2023).
- [22] V. Klüsener, S. Pucher, D. Yankelev, J. Trautmann, F. Spriestersbach, D. Filin, S. Porsev, M. Safronova, I. Bloch, and S. Blatt, Long-lived coherence on a μHz scale optical magnetic quadrupole transition, *Phys. Rev. Lett.* **132**, 253201 (2024).
- [23] S. Pucher, V. Klüsener, F. Spriestersbach, J. Geiger, A. Schindewolf, I. Bloch, and S. Blatt, Fine-structure qubit encoded in metastable strontium trapped in an optical lattice, *Phys. Rev. Lett.* **132**, 150605 (2024).
- [24] G. Unnikrishnan, P. Ilzhöfer, A. Scholz, C. Hölzl, A. Götzelmann, R. Gupta, J. Zhao, J. Krauter, S. Weber, N. Makki, H. Büchler, T. Pfau, and F. Meinert, Coherent control of the fine-structure qubit in a single alkaline-earth atom, *Phys. Rev. Lett.* **132**, 150606 (2024).
- [25] M. Norcia, A. Young, and A. Kaufman, Microscopic control and detection of ultracold strontium in optical-tweezer arrays, *Phys. Rev. X* **8**, 041054 (2018).
- [26] T. Ido and H. Katori, Recoil-free spectroscopy of neutral sr atoms in the lamb-dicke regime, *Phys. Rev. Lett.* **91**, 053001 (2003).
- [27] R. Yamamoto, J. Kobayashi, T. Kuno, K. Kato, and Y. Takahashi, An ytterbium quantum gas microscope with narrow-line laser cooling, *New J. Phys.* **18**, 023016 (2016).
- [28] A. Cooper, J. P. Covey, I. S. Madjarov, S. G. Porsev, M. S. Safronova, and M. Endres, Alkaline-earth atoms in optical tweezers, *Phys. Rev. X* **8**, 041055 (2018).
- [29] A. Taichenachev, V. Yudin, C. Oates, C. Hoyt, Z. Barber, and L. Hollberg, Magnetic field-induced spectroscopy of forbidden optical transitions with application to lattice-based optical atomic clocks, *Phys. Rev. Lett.* **96**, 083001 (2006).
- [30] T. Hong, C. Cramer, W. Nagourney, and E. N. Fortson, Optical clocks based on ultranarrow three-photon resonances in alkaline earth atoms, *Phys. Rev. Lett.* **94**, 050801 (2005).
- [31] J. He, B. Pasquiou, R. G. Escudero, S. Zhou, M. Borkowski, and F. Schreck, Coherent three-photon excitation of the strontium clock transition, *arXiv:2406.07530* (2024).
- [32] S. P. Carman, J. Rudolph, B. E. Garber, M. J. V. de Graaff, H. Swan, Y. Jiang, M. Nantel, M. Abe, R. L. Barcklay, and J. M. Hogan, Collinear three-photon excitation of a strongly forbidden optical clock transition, *arXiv:2406.07902* (2024).
- [33] H. Levine, D. Bluvstein, A. Keesling, T. T. Wang, S. Ebadi, G. Semeghini, A. Omran, M. Greiner, V. Vuletić, and M. D. Lukin, Dispersive optical systems for scalable raman driving of hyperfine qubits, *Phys. Rev. A* **105**, 032618 (2022).
- [34] D. Bluvstein, S. J. Evered, A. A. Geim, S. H. Li, H. Zhou, T. Manovitz, S. Ebadi, M. Cain, M. Kalinowski, D. Hangleiter, J. P. Bonilla Ataides, N. Maskara, I. Cong, X. Gao, P. Sales Rodriguez, T. Karolyshyn, G. Semeghini, M. J. Gullans, M. Greiner, V. Vuletić, and M. D. Lukin, Logical quantum processor based on reconfigurable atom arrays, *Nature* **626**, 58 (2024).
- [35] M. Takamoto, F.-L. Hong, R. Higashi, and H. Katori, An optical lattice clock, *Nature* **435**, 321–324 (2005).
- [36] A. D. Ludlow, M. M. Boyd, T. Zelevinsky, S. M. Foreman, S. Blatt, M. Notcutt, T. Ido, and J. Ye, Systematic study of the ^{87}Sr clock transition in an optical lattice, *Phys. Rev. Lett.* **96**, 033003 (2006).
- [37] J. P. Covey, I. S. Madjarov, A. Cooper, and M. Endres, 2000-times repeated imaging of strontium atoms in clock-magic tweezer arrays, *Phys. Rev. Lett.* **122**, 173201 (2019).
- [38] H. Ball, W. D. Oliver, and M. J. Biercuk, The role of master clock stability in quantum information processing, *npj Quantum Inf.* **2**, 16033 (2016).
- [39] J. H. Bodey, R. Stockill, E. V. Denning, D. A. Gangloff, G. Éthier Majcher, D. M. Jackson, E. Clarke, M. Hugues, C. L. Gall, and M. Atatüre, Optical spin locking of a solid-state qubit, *npj Quantum Inf.* **5**, 95 (2019).
- [40] M. Bishof, X. Zhang, M. J. Martin, and J. Ye, Optical spectrum analyzer with quantum-limited noise floor, *Phys. Rev. Lett.* **111**, 093604 (2013).
- [41] M. L. Day, P. J. Low, B. White, R. Islam, and C. Senko, Limits on atomic qubit control from laser noise, *npj Quantum Inf.* **8**, 72 (2022).
- [42] H. Nakav, R. Finkelstein, L. Peleg, N. Akerman, and R. Ozeri, Effect of fast noise on the fidelity of trapped-ion quantum gates, *Phys. Rev. A* **107**, 042622 (2023).
- [43] S. Heußen, D. F. Locher, and M. Müller, Measurement-free fault-tolerant quantum error correction in near-term devices, *PRX Quantum* **5**, 010333 (2024).
- [44] J. T. Barreiro, M. Müller, P. Schindler, D. Nigg, T. Monz, M. Chwalla, M. Hennrich, C. F. Roos, P. Zoller, and R. Blatt, An open-system quantum simulator with trapped ions, *Nature* **470**, 486 (2011).
- [45] T. Ishiyama, K. Ono, T. Takano, A. Sunaga, and Y. Takahashi, Observation of an inner-shell orbital clock transition in neutral ytterbium atoms, *Phys. Rev. Lett.* **130**, 153402 (2023).
- [46] M. S. Safronova, D. Budker, D. DeMille, D. F. J. Kimball, A. Derevianko, and C. W. Clark, Search for new physics with atoms and molecules, *Rev. Mod. Phys.* **90**, 025008 (2018).
- [47] A. Heinz, A. Park, N. Šantić, J. Trautmann, S. Porsev, M. Safronova, I. Bloch, and S. Blatt, State-dependent optical lattices for the strontium optical qubit, *Phys. Rev. Lett.* **124**, 203201 (2020).
- [48] F. Reiter and A. S. Sørensen, Effective operator formalism for open quantum systems, *Phys. Rev. A* **85**, 032111 (2012).
- [49] B. E. King, Angular momentum coupling and rabi frequencies for simple atomic transitions (2008), *arXiv:0804.4528*.
- [50] J. D. Thompson, T. G. Tiecke, A. S. Zibrov, V. Vuletić, and M. D. Lukin, Coherence and raman sideband cooling of a single atom in an optical tweezer, *Phys. Rev. Lett.* **110**, 133001 (2013).
- [51] B. Richards and E. Wolf, Electromagnetic diffraction in optical systems, II. structure of the image field in an aplanatic system, *Proc. R. Soc. Lond.* **253**, 358 (1959).
- [52] A. W. Young, W. J. Eckner, N. Schine, A. M. Childs, and A. M. Kaufman, Tweezer-programmable 2d quantum walks in a hubbard-regime lattice, *Science* **377**, 885–889 (2022).

- [53] S. Buob, J. Höschele, V. Makhalov, A. Rubio-Abadal, and L. Tarruell, A strontium quantum-gas microscope, *PRX Quantum* **5**, 020316 (2024).
- [54] R. Tao, M. Ammenwerth, F. Gyger, I. Bloch, and J. Zeiher, High-fidelity detection of large-scale atom arrays in an optical lattice, *Phys. Rev. Lett.* **133**, 013401 (2024).
- [55] F. Gyger, M. Ammenwerth, R. Tao, H. Timme, S. Snigirev, I. Bloch, and J. Zeiher, Continuous operation of large-scale atom arrays in optical lattices, *Phys. Rev. Res.* **6**, 033104 (2024).